photonics

MDPI

Article

Asymmetrical Three-Dimensional Conformal Imaging Lens

Desen Gong, Yixiao Ge, Wen Xiao * and Huanyang Chen *

Department of Physics, Institute of Electromagnetics and Acoustics, Xiamen University, Xiamen 361005, China; 19820211153673@stu.xmu.edu.cn (D.G.); 34320200155780@stu.xmu.edu.cn (Y.G.)
* Correspondence: xiaowen@xmu.edu.cn (W.X.); kenyon@xmu.edu.cn (H.C.)

Abstract: Absolute instrument refers to a media that can make light rays to propagate in a closed orbit and perform imaging and self-imaging. In the past few decades, traditional investigations into absolute instrument have been centered on the two-dimensional plane and rotational symmetry situations, and have paid less attention to three-dimensional counterparts. In this article, we design two types of three-dimensional non-spherically symmetric absolute instruments based on conformal inverse transformation, which originated from the three-dimensional Luneburg lens and Lissajous lens. We carry out ray tracing on the optical performance of these new lenses and analyze the imaging laws. Our work enlarges the family of absolute instruments from two dimensions to three dimensions and symmetry to asymmetry, which may allow for imaging applications in optical waves.

Keywords: three-dimensional conformal transformation; absolute instruments; inverse mapping; non-spherical symmetry

1. Introduction

The flourishing of transformation optics (TO) can be traced back to two pioneering papers published in *Science* in 2006. In these papers, Leonhardt and Pendry et al. proposed theories for constructing invisibility cloaks based on optical conformal mapping and coordinate transformations, respectively. Over the past two decades, TO has yielded numerous novel applications, including invisibility cloaks [1,2], field rotators [3,4], and super-scattering phenomena [5]. Leveraging the form invariant of Maxwell's equations under coordinate transformations, TO has extended its utility to astronomical analogies, enabling the mimicking of celestial phenomena such as black holes [6], wormholes [7,8], and Einstein rings [9]. Among the diverse applications of TO, optical imaging stands out as a prominent one. Distinguishing itself from Pendry's proposal that the negative refractive index makes for perfect imaging [10] (though it can also be viewed as a form of folding transformation in TO), imaging investigations within TO predominantly rely on positive refractive index imaging systems. Although Leondhart's proposition that Maxwell's fish-eye lens could achieve perfect imaging in wave optics stirred some controversy [11–16], it did not impede the development of imaging research within geometric optics in the context of TO.

TO has the potential to broaden the applicability of gradient refractive index lenses, exemplified by Maxwell's fish-eye lens [17] and the Luneburg lens [18], and theoretically enrich imaging lenses. Such imaging lenses, capable of producing aberration-free images of a region in space, are denoted as absolute instruments (AIs) [19]. AIs offer lots of opportunities for super-imaging, as achieving super-resolution entails capturing as much light as possible, including propagating and evanescent waves [10,20]. It is important to note that the imaging mechanism of AIs here is different from that of antenna arrays [21] or phase-controlled [22] imaging mechanisms. AIs are characterized by perfect geometric imaging and do not take the diffraction field into account. In addition to Maxwell's fish-eye lens, planar mirrors, and negative refractive index lenses, Miñano has identified Luneburg lenses and Eaton lenses as types of AIs [23]. The Mikaelian lens (independently proposed

check for updates

Citation: Gong, D.; Ge, Y.; Xiao, W.; Chen, H. Asymmetrical Three-Dimensional Conformal Imaging Lens. *Photonics* **2024**, *11*, 543. https://doi.org/10.3390/photonics11060543

Received: 6 May 2024
Revised: 1 June 2024
Accepted: 4 June 2024
Published: 7 June 2024

Copyright: © 2024 by the authors. Licensee MDPI, Basel, Switzerland. This article is an open access article distributed under the terms and conditions of the Creative Commons Attribution (CC BY) license (https://creativecommons.org/licenses/by/4.0/).

in 1951) is a conformal-mapping lens derived from Maxwell's fish-eye lens and qualifies as an AI [24,25]. Chen et al. introduced the Morse lens based on the Morse potential, serving as a valuable augmentation to one-dimensional (1D) AIs [26]. Because of the periodic and closed orbit characteristics of light rays in AIs, Tyc et al. performed a frequency analysis and discovered that the frequency spectra are spaced almost equally [27,28], and then concluded that the AIs are actually good superintegrability systems [29]. Subsequently, the generalized methodology for designing rotationally symmetric AIs has been proposed [30]. Recent works in the literature have included reports on geodesic lenses associated with the AIs [31,32]. Geodesic lenses are two-dimensional (2D) curved surfaces in three-dimensional (3D) space, corresponding to the gradient refractive index media based on geodesic conformal transformation [33]. Nevertheless, the majority of AI investigations are confined to scenarios characterized by high symmetry, such as rotationally symmetric or spherically symmetric configurations. Although asymmetric 2D or 3D AIs have been documented [23,34], their exploration and applications remain ambiguous.

In this letter, we investigate 3D non-spherically symmetric AIs based on conformal mapping. Given the limited variety of 3D conformal transformation, we exemplify our study with inverse transformation and illustrate asymmetric AIs stemming from Luneburg and Lissajous lenses. Starting from the 2D case, we verify the form invariance of the scalar Helmholtz equation under inverse transformation in 3D space and derive the analytical forms of non-spherically symmetric AIs. Furthermore, we conduct an analysis of their imaging characteristics, utilizing geometric ray tracing based on Hamilton's equations. Our findings provide valuable insights for advancing 3D imaging methodologies.

2. Results and Discussion

According to Liouville's theorem, in 3D space, only the Mobius transformations are conformal, and they are limited to translations, similarities, rotations, and inversions, which have very limited applications in TO [35]. It can be noted that there are some applications based on 3D quasi-conformal mapping, which is not within the scope of our consideration [36,37]. For the inverse conformal transformation, $w = 1/z$, where w represents the 2D virtual space coordinate system $w : \{u, v\}(w = u + iv)$ and z represents the 2D physical space coordinate system $z : \{x, y\}$ $(z = x + iy)$. The coordinate correspondence between the virtual space and the physical space in the 2D case satisfied the Cauchy–Riemann relations [38]:

$$u = \frac{x}{x^2 + y^2}, v = -\frac{y}{x^2 + y^2}. \tag{1}$$

We emphasize that here, u, v, x, and y all have dimensions of length; that is, the relationship expressed in Equation (1) is only quantitative. As there are no Cauchy–Riemann equations in 3D, we conjecture that the coordinate correspondence between the two spaces of the inverse conformal transformation in the 3D case is

$$u = \pm\frac{x}{x^2 + y^2 + z^2}, v = \pm\frac{y}{x^2 + y^2 + z^2}, w = \pm\frac{z}{x^2 + y^2 + z^2}. \tag{2}$$

The above is the correspondence between the virtual space coordinate system $P : \{u, v, w\}$ and the physical space coordinate system $Q : \{x, y, z\}$. We define the refractive index distributions of the virtual space as $n_P(u, v, w)$ and the physical space as $n_Q(x, y, z)$, respectively. Analogous to the 2D Cauchy–Riemann conditions in Equation (1), there are eight combinations of 3D inverse transformations, as presented in Equation (2). These combinations can result in the emergence of positive and negative refractive indices $n_Q(x, y, z)$ after inverse mapping. A positive refractive index indicates that the inversion preserves both the angle and the orientation, while a negative refractive index indicates that the inversion preserves the angle but reverses the orientation, and they are both isotropic. Since all the lenses we consider in this paper fill the entire space, the choice of positive or negative refractive indices does not change the trajectory of the light rays. Therefore, our subsequent studies will focus on the imaging principles of inverse lenses with the

positive refractive index. In addition, the transformed isotropic refractive index $n_Q(x,y,z)$ can be also obtained based on the optical path invariance [38], between the physical space and the virtual space, i.e., $n_p(u,v,w)^2(du^2+dv^2+dw^2) = n_Q(x,y,z)^2(dx^2+dy^2+dz^2)$, by choosing the positive index. The optical path length along a certain route in physical space are as follows:

$$s_Q = \int n_Q(x,y,z)\sqrt{dx^2+dy^2+dz^2}. \tag{3}$$

And the optical path length in virtual space are

$$\begin{aligned} &s_p = \int n_P(u,v,w)\sqrt{du^2+dv^2+dw^2} \\ &= \int n_P(u,v,w)[(\frac{\partial u}{\partial x}dx+\frac{\partial u}{\partial y}dy+\frac{\partial u}{\partial z}dz)^2+(\frac{\partial v}{\partial x}dx+\frac{\partial v}{\partial y}dy+\frac{\partial v}{\partial z}dz)^2 \\ &+(\frac{\partial w}{\partial x}dx+\frac{\partial w}{\partial y}dy+\frac{\partial w}{\partial z}dz)^2]^{1/2}. \end{aligned} \tag{4}$$

Substituting Equation (2) into Equation (3) and calculating will produce

$$\begin{aligned} &\int n_P(u,v,w)\sqrt{du^2+dv^2+dw^2} \\ &= \int n_P(u,v,w)\sqrt{dx^2+dy^2+dz^2}/(x^2+y^2+z^2). \end{aligned} \tag{5}$$

Keeping the optical path unchanged during mapping gives

$$\int n_Q(x,y,z)\sqrt{dx^2+dy^2+dz^2} = \int n_P(u,v,w)\sqrt{du^2+dv^2+dw^2}. \tag{6}$$

Finally, in this way, we obtain a result for the isotropic media parameters' corresponding relationship $n_Q(x,y,z) = n_p(u,v,w)/(x^2+y^2+z^2)$, which is very similar to the refractive index induced by the 2D inverse conformal transformation in Equation (1), namely $n_{q1}(x,y) = n_{p1}(u,v)/(x^2+y^2)$; we confirm that Equation (2) is the correct form of the 3D inverse conformal transformation. The lowercase $q1$ and $p1$ represent the 2D virtual space and physical space, respectively.

We can now evidence the scalar form invariance of the Helmholtz equation under the transformations in Equation (2). The Helmholtz equations are written separately for physical space $Q:\{x,y,z\}$ and virtual space $P:\{u,v,w\}$:

$$(\nabla^2+n_Q^2k^2)A = 0, (\nabla'^2+n_P^2k^2)A = 0. \tag{7}$$

In Equation (7), k is the wavevector and A is the electromagnetic wave amplitude (it can also be the acoustic wave or matter wave amplitude). The Laplace operator for two spaces can be written as

$$\nabla^2 = \frac{\partial^2}{\partial x^2}+\frac{\partial^2}{\partial y^2}+\frac{\partial^2}{\partial z^2}, \nabla'^2 = \frac{\partial^2}{\partial u^2}+\frac{\partial^2}{\partial v^2}+\frac{\partial^2}{\partial w^2}, \tag{8}$$

And it is known that

$$\frac{\partial}{\partial x_i} = \frac{\partial}{\partial u}\frac{\partial u}{\partial x_i}+\frac{\partial}{\partial v}\frac{\partial v}{\partial x_i}+\frac{\partial}{\partial w}\frac{\partial w}{\partial x_i}(x_i = x,y,z). \tag{9}$$

Ultimately, we combine Equations (2), (8), and (9) to obtain the relationship between the Laplace operators of the two spaces, as follows:

$$\nabla^2 = \frac{1}{(x^2+y^2+z^2)^2}(\frac{\partial^2}{\partial u^2}+\frac{\partial^2}{\partial v^2}+\frac{\partial^2}{\partial w^2}) = \frac{1}{(x^2+y^2+z^2)^2}\nabla'^2, \tag{10}$$

Combining Equation (7) with Equation (10), in order to reflect the form invariance of the Helmholtz equation, the relationship between the Laplace operators of the two spaces

can be equated to the relationship between the refractive indices of the two spaces: $n_Q(x, y, z) = n_p(u, v, w)/(x^2 + y^2 + z^2)$, which gets same result of Equation (2). Therefore, we demonstrate the form invariance of the Helmholtz equations under the inverse transformation. Here, we also choose the positive one, as the choice of sign does not affect our results and conclusions.

Next, we apply 3D inverse conformal transformation as well as the 2D inverse conformal transformation to the two AIs, i.e., the Luneburg lens and the Lissajous lens. We first move the center (0, 0) of the 2D and 3D Luneburg lens to (x_0, y_0) and (x_0, y_0, z_0). This translation will not affect the rotational symmetry and spherical symmetry of the Luneburg lens, but after the inverse transformation, the imaging trajectories will become non-spherically symmetric but still are AIs. The Lissajous lenses do not need to make any adjustments before inversion, because they already lack rotational or spherical symmetry. The two types of gradient refractive index lens and their 2D and 3D refractive index distribution are

$$n = \sqrt{2 - (x - x_0)^2 - (y - y_0)^2}, \tag{11}$$

$$n = \sqrt{2 - (x - x_0)^2 - (y - y_0)^2 - (z - z_0)^2}, \tag{12}$$

$$n = \sqrt{2 - \frac{x^2}{a^2} - \frac{y^2}{b^2}}, \tag{13}$$

$$n = \sqrt{2 - \frac{x^2}{a^2} - \frac{y^2}{b^2} - \frac{z^2}{c^2}}. \tag{14}$$

Equations (11) and (12) are 2D and 3D Luneburg lenses and Equations (13) and (14) are 2D and 3D Lissajous lenses, $x_0,\ y_0,\ z_0 \in [0, 1)$; a, b, and c are generally non-zero integers. After performing the corresponding inverse transformation proposed in Equation (2), respectively, the refractive index of these two types of lenses in physical space are

$$n_z = \sqrt{2 - \left(\frac{x}{r_z^2} - x_0\right)^2 - \left(-\frac{y}{r_z^2} - y_0\right)^2} \Big/ r_z^2, \tag{15}$$

$$n_Q = \sqrt{2 - \left(\frac{x}{r_Q^2} - x_0\right)^2 - \left(\frac{y}{r_Q^2} - y_0\right)^2 - \left(\frac{z}{r_Q^2} - z_0\right)^2} \Big/ r_Q^2, \tag{16}$$

$$n_z = \sqrt{\frac{2}{r_z^4} - \frac{x^2}{a^2 r_z^8} - \frac{y^2}{b^2 r_z^8}}, \tag{17}$$

$$n_Q = \sqrt{\frac{2}{r_Q^4} - \frac{x^2}{a^2 r_Q^8} - \frac{y^2}{b^2 r_Q^8} - \frac{z^2}{c^2 r_Q^8}}. \tag{18}$$

In Equations (15)–(18), $r_z^2 = x^2 + y^2$, $r_Q^2 = x^2 + y^2 + z^2$. Here, we implement the ray tracing calculations based on Hamilton's equations [38–40], $\frac{d\boldsymbol{r}}{dt} = \frac{\partial \omega}{\partial \boldsymbol{k}}$, $\frac{d\boldsymbol{k}}{dt} = -\frac{\partial \omega}{\partial \boldsymbol{r}}$, where $\boldsymbol{r}$ is the position vector, $\boldsymbol{k}$ is the wave vector, and ω donates the angular frequency. Combined with the dispersion in the isotropic gradient media $\omega = \frac{ck}{n}$ (c is the light speed and n is the refractive index profile), the Hamilton's equations will finally become $\frac{d\boldsymbol{r}}{dt} = -\frac{c}{n}\frac{\boldsymbol{k}}{|\boldsymbol{k}|}$, $\frac{\partial \boldsymbol{k}}{dt} = \frac{c|\boldsymbol{k}|}{n^2}\nabla n$. We have attached the corresponding matlab code at the end of the main text. In all the cases that follow, the point sources are all set at (1, 0) or (1, 0, 0) points. First, we show the schematic diagrams of ray trajectories in Equation (11) and its counterpart Equation (15) in Figure 1.

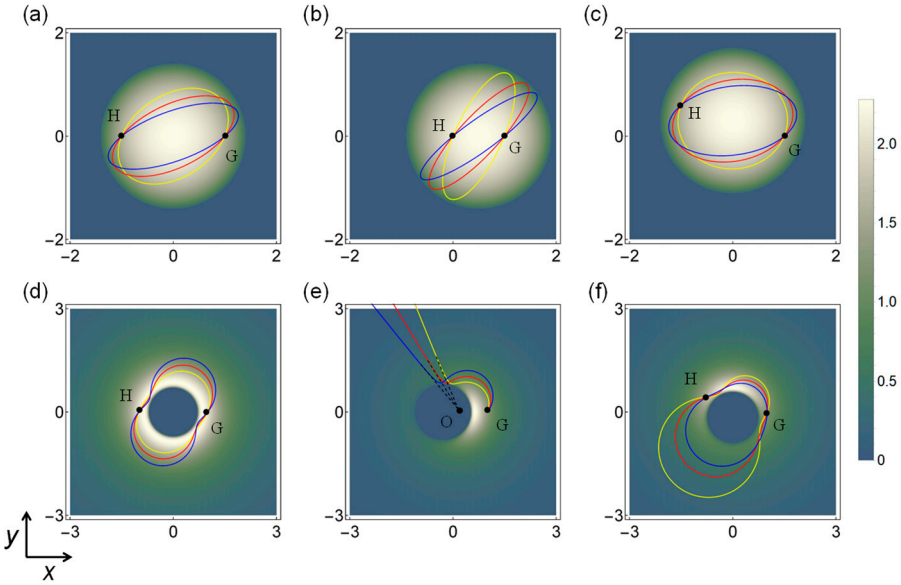

Figure 1. Schematic simulation of refractive index distribution and ray tracing for 2D Luneburg lens and 2D inverse Luneburg lens: (**a**–**c**) show the cases of the Luneburg lens with $x_0 = 0, y_0 = 0$; $x_0 = 0.5, y_0 = 0$; and $x_0 = 0, y_0 = 0.3$; (**d**–**f**) show inverse Luneburg lens with $x_0 = 0, y_0 = 0$; $x_0 = 0.5, y_0 = 0$; and $x_0 = 0, y_0 = 0.3$. Here, x_0, y_0 have dimensions of length, they are arbitrary units, and as long as the geometric optics approximation is satisfied, the system can be scaled. The color bar on the right shows the refractive index at the location of the corresponding color in the subfigures. All point sources in these six figures are placed at point G (1, 0). The point H labeled in (**a**–**d**,**f**) is another imaging point in addition to the point source G. After making a reverse extension of the straight-line segments of the three rays in (**e**), it is found that the extension lines intersect at the origin.

The different translations with 2D Luneburg lenses are illustrated in Figure 1a–c, where the regions with positive refractive index are located within a circle of radius $\sqrt{2}$, while outside the circle, the refractive index is imaginary. In a Luneburg lens distributed throughout space, the trajectories of light rays starting from point G form ellipses, join the imaging point H, and come back to point G. The variations in x_0 and y_0 in Equation (11) cause the changes in the position of the imaging point H. In Figure 1a, point H is located at $(-1, 0)$, in Figure 1b at $(0, 0)$, and in Figure 1c at $(-1, 0.6)$. After the inverse conformal transformation, the region with imaginary refractive index is included within the central circle of radius $\sqrt{2}/2$, as shown in Figure 1d–f, and when light rays approach the boundary near this region, they are reflected away. In Figure 1d, the imaging point is at H $(-1, 0)$, while in the scenario shown in Figure 1e, there is no imaging point, or it can be said that the imaging point is at infinity. This is because before the inverse transformation, the imaging point is at the origin, and after the inverse transformation, it goes to infinity. If the straight-line portions of these light ray trajectories are extended backward, they intersect at the origin, which could likely cause a visual illusion: the point source actually lies at point G, but to an observer far away, the point source appears to be at the origin. From Figure 1e,f, it can be observed that the translation operation in virtual space disrupts the rotational symmetry of the inverse Luneburg lens refractive index distribution, causing the regions with higher refractive index to gradually become crescent-shaped and attached to one side of the circular region with imaginary refractive index.

Let us move on to the 2D Lissajous lens and its inverse mapping lens, as shown in Figure 2. From the refractive index distribution in Figure 2a–c, it can be observed that compared to the Luneburg lens, the positive refractive index region of the Lissajous lens is stretched into an ellipse. The orientation of the major axis of the ellipse depends on the relative sizes of parameters a and b: if a is larger, it points towards the x-axis, and if b is larger, it points towards the y-axis. In a Lissajous lens, the trajectory of light rays forms a Lissajous figure, hence its name. In Figure 2a, there is only one imaging point

located at point G. In Figure 2b,c, there are two imaging points: one at the source point G and the other at point H. The number of imaging points in a Lissajous lens depends on the position of the source point and the ratio of a to b, and, if a Lissajous lens exists with two imaging points, the symmetrical forms between these two imaging points feature symmetry about the origin, symmetry about the x-axis, and symmetry about the y-axis. These patterns can all be analogized by combining the light trajectory of the Lissajous lens with the synthesis of anisotropic harmonic oscillations in two perpendicular directions, inspired by the optical–mechanical analogy [23,41]. In Figure 2d–f, the number of imaging points are 1, 2, and 2, respectively. It can be observed that the central portion of the inverse Lissajous lens resembles a peanut-shaped region, where the refractive index values are imaginary, with the boundary of the region having a refractive index of zero. The regions with higher refractive index are symmetrically distributed around the waist of the peanut. Compared to the Lissajous lens, the maximum value of refractive index in the inverse Lissajous lens is significantly increased. Additionally, the inverse conformal transformation does not disrupt the imaging characteristics of the Lissajous lens, including the number of imaging points and the symmetry between imaging points when there are multiple ones. Therefore, when inferring the imaging characteristics of the inverse Lissajous lens, we can directly use the analogy of harmonic oscillations in the Lissajous lens based on inverse transformation, and the results will be the same.

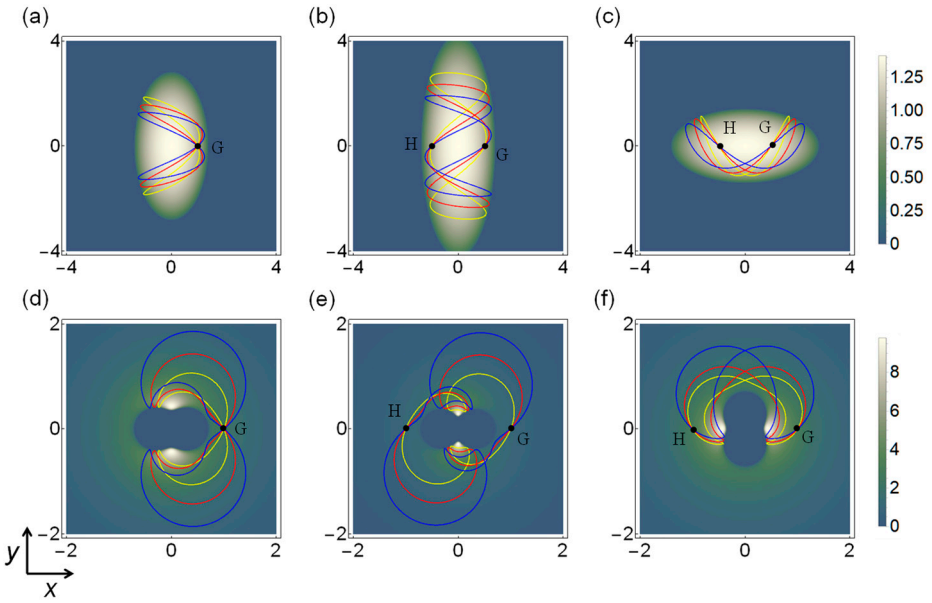

Figure 2. Schematic simulation of refractive index distribution and ray tracing for the 2D Lissajous lens and 2D inverse Lissajous lens: (**a**–**c**) show the cases of the Lissajous lens with $a = 1, b = 2$; $a = 1, b = 2$; and $a = 2, b = 1$; (**d**–**f**) show inverse Lissajous lens with $a = 1, b = 2$; $a = 1, b = 2$; and $a = 2, b = 1$. The color bar on the right side of (**c**) displays the refractive index at the corresponding color positions in (**a**–**c**), while the color bar on the right side of (**f**) displays the refractive index at the corresponding color positions in (**d**–**f**). All point sources in these six figures are placed at point G (1,0).

After covering the asymmetric lens scenario in 2D, we can analyze the construction of 3D non-spherically symmetric AIs. We also studied the 3D Luneburg lens first. From Figure 3, with the inverse 3D Luneburg lens, we can see that when the point source is placed at G (1, 0, 0), translations in the y and z directions cause only imaging point H to move in the corresponding direction. Only when there is a certain degree of eccentricity in the x direction, as shown in Figure 3b, do the light trajectories no longer close, and there are no imaging points. Further investigation reveals that the extensions of each light ray intersect at the origin, leading to optical illusion phenomena similar to those shown in Figure 1e.

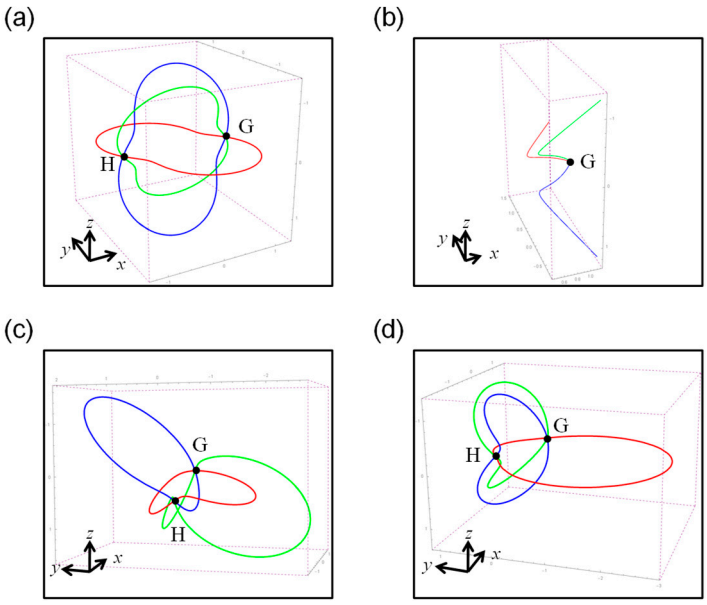

Figure 3. Ray tracing calculations of 3D inverse Luneburg lenses under various translation conditions: (**a**–**d**) show the cases of the inverse Luneburg lens with $x_0 = 0, y_0 = 0, z_0 = 0$; $x_0 = 0.5, y_0 = 0, z_0 = 0$; $x_0 = 0, y_0 = 0, z_0 = 0.5$; and $x_0 = 0, y_0 = 0.5, z_0 = 0$, respectively. In all four subfigures, the point sources are placed at point G (1, 0, 0), with the directions of the three coordinate axes indicated in the bottom left corner of each diagram.

As for the Lissajous lens, we illustrate the ray trajectories in Figure 4. It can be seen that the point source is placed at G (1, 0, 0), and the trajectories of all light rays still form Lissajous patterns in the six plots of Figure 4. This phenomenon is related to the selection of the point source location and the ratios of a, b, and c. However, as long as the ratios of any two of a, b, and c satisfy the conditions of being non-irrational and non-infinite, the 3D Lissajous lens is a class of AI [23]. Moreover, it is one of the few non-spherically symmetric AIs in 3D space. The initial directions of the three light rays emitted from point source G form acute angles with the negative direction of the x-axis. The positions where the light rays intersect during propagation correspond to the locations of the imaging points. In Figure 4a–f, the imaged points other than the point source G are labeled H, and it can be seen that the number of imaged points for the six cases are 1, 2, 1, 2, 2, and 2, respectively. Regarding the imaging law of the Lissajous lens, it has been pointed out that the 3D Lissajous lens corresponds to the interaction potential of a 3D anisotropic harmonic oscillator based on the optical–mechanical analogy [23], and here we regard the ray trajectory of the 3D Lissajous lens as the synthesis of simple harmonic oscillations in three mutually perpendicular directions x, y, and z; then, the analytical formula of the simple harmonic oscillation in each direction is

$$\begin{cases} x = x_0 \cos(t/a) + A \sin(t/a) \\ y = y_0 \cos(t/b) + B \sin(t/b) \\ z = z_0 \cos(t/c) + C \sin(t/c) \end{cases}, \tag{19}$$

where (x_0, y_0, z_0) represents the coordinates of the point source, $[A, B, C]$ is the direction vector of the light ray when it is emitted from the point source, and t is the time parameter. In this way, we can calculate the number of imaging points and the coordinates of a three-dimensional Lissajous lens after knowing its parameters a, b, and c and the location of the point source inside the lens. For example, the calculations of ray tracing inside the 3D Lissajous lens are shown in Figure 5a when $a = 1, b = 2, c = 3$ and the coordinates of the point source are (1, 1, 1), and the function image drawn after substituting the above parameters into Equation (19) is shown in Figure 5b.

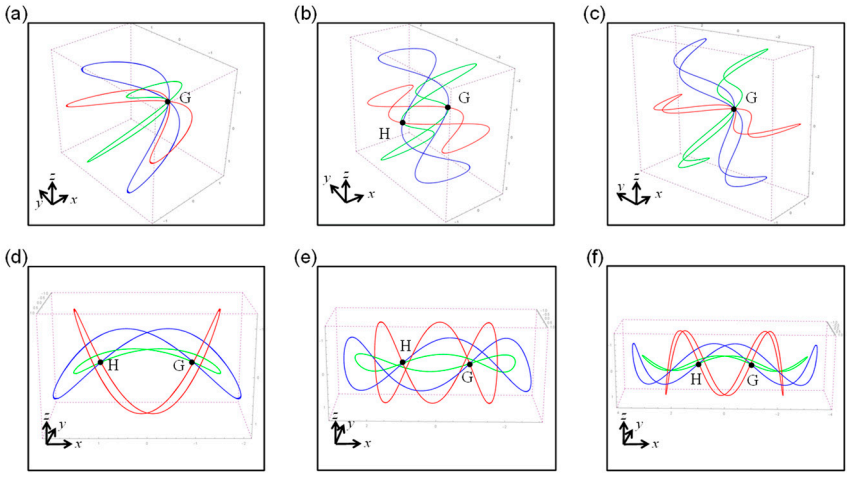

Figure 4. Ray tracing calculations of the 3D Lissajous lens under different parameter conditions: (**a**–**f**) show the cases of the Lissajous lens with $a = 1, b = 2, c = 2$; $a = 1, b = 3, c = 3$; $a = 1, b = 4, c = 4$; $a = 2, b = 1, c = 1$; $a = 3, b = 1, c = 1$; and $a = 4, b = 1, c = 1$, respectively. In all subfigures, the point sources are placed at point G (1, 0, 0), with the directions of the three coordinate axes indicated in the bottom left corner of each diagram.

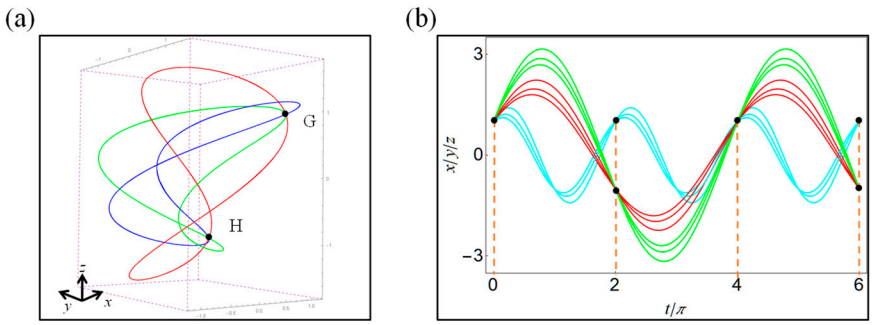

Figure 5. (**a**) The 3D Lissajous lens ray trajectories with the cases of $a = 1, b = 2, c = 3$ where the point source is located in G (1, 1, 1); all the ray trajectories are a closed three-dimensional space curve, and the imaging points are the G point and H point. (**b**) The plots of x, y, z as a function of the parameter t obtained by substituting the values of the above parameters into Equation (19) are shown in blue for x, red for y, and green for z. There are three function curves of each color because the direction vectors [A, B, C] are taken in the three cases of [1, 2, 3], [0.5, 1.5, 2.5], and [0.7, 1.7, 2.7].

According to the 3D Lissajous lens parameters and point source coordinates and other information, combined with Equation (19) to draw the function image in Figure 5b, at this time, the black point on the curve in the figure of the longitudinal coordinates is the coordinates of the imaging point in the lens under the above conditions. From Figure 5b, it can be seen that when the value of t is an even multiple of 2π, the specific coordinates of the imaging point are (1, 1, 1), and when the value of t is an odd multiple of 2π, the coordinates of the imaging point are $(1, -1, -1)$. This gives the coordinates of point H in Figure 5a as $(1, -1, -1)$. By plotting the graph of the function and analyzing it, we are able to get the number of image points as well as the coordinates. and summarize the relevant laws: when $t = N\pi$, there is an imaging point (N is the least common multiple for a, b and c). When there are two imaging points, the symmetry of the two imaging points is symmetric about the three coordinate axes, symmetric about the three coordinate planes, and symmetric about the origin, which makes seven kinds of symmetry.

Now, let us explore the 3D inverse Lissajous lens for the case with six combinations of different a, b, c values in the illustration in Figure 6, which is also without spherical symmetry. We have already learned about the specificity of the refractive index distribution of the inverse Lissajous lens in the 2D case, and the complexity of the refractive index

distribution of this lens increases as the spatial dimensionality increases. In the six diagrams of Figure 6, the three rays labeled with red, green, and blue are all emitted from point G (1, 0, 0), and the angles between the initial directions of the rays and the negative direction of the x-axis are also acute angles. The parameters of the six images in Figure 6 are the same as those of the corresponding images in Figure 5, and the number of final imaging points also corresponds exactly. It can be seen that the 3D inverse conformal transformation we derived also does not destroy the imaging properties of the Lissajous lens, and the number of imaging points and the symmetry between the imaging points in the case of multiple imaging points are exactly the same before and after the 3D inverse conformal transformation, and then Equation (19) can be used to predict the distribution of the imaging points of the 3D inverse Lissajous lens, as well. In this way, 3D inversion Lissajous lenses have been successfully incorporated into the family of aspherical symmetric AIs.

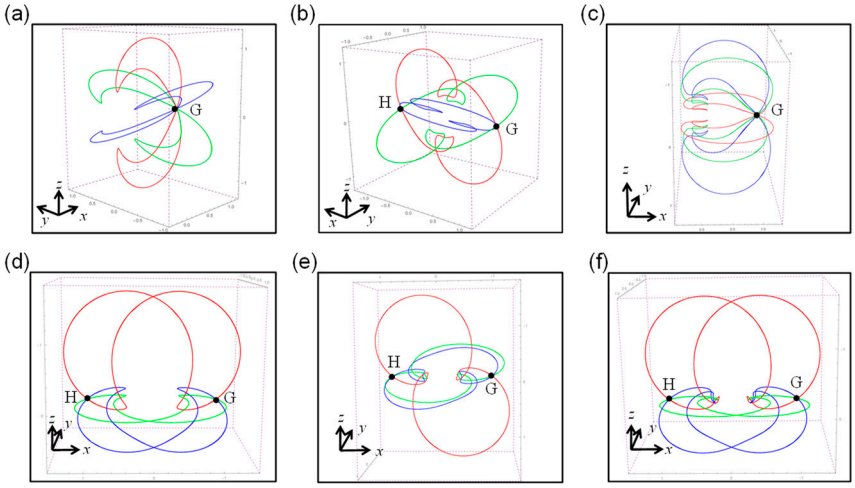

Figure 6. Ray tracing calculation of 3D inverse Lissajous lenses under different parameter conditions: (**a**–**f**) show the cases of the inverse Lissajous lens with $a = 1, b = 2, c = 2$; $a = 1, b = 3, c = 3$; $a = 1, b = 4, c = 4$; $a = 2, b = 1, c = 1$; $a = 3, b = 1, c = 1$; and $a = 4, b = 1, c = 1$. The point sources are placed at point G (1, 0, 0), with the directions of the three coordinate axes indicated in the bottom left corner of each diagram.

3. Conclusions

In summary, we investigate 3D non-spherically symmetric AIs through the framework of conformal mapping. By focusing on the inverse transformation and employing Luneburg and Lissajous lenses as illustrative examples, we showcase the emergence of asymmetric AIs. We confirm the form invariance of the scalar Helmholtz equation's form under inversion transformation in 3D space, and we use Hamiltonian optics to analyze their imaging characteristics with geometric rays. Note that in wave optics, those lenses can also perform imaging (although not perfectly) under the geometric optics approximations, but the imaging effect is limited by the diffraction limit because the lens cannot collect evanescent waves during imaging. Our work extends the scope of AIs into 3D space, introducing asymmetry alongside symmetry, and has the potential to drive further progress in the development of 3D imaging methodologies. Finally, it is necessary to discuss the possible experimental preparation and application prospects of 2D and 3D lenses. Of all the lenses mentioned in this article, the Luneburg lens is currently the most widely used, with many applications in both 2D and 3D, such as wireless communication [42], radar systems [43], and optical focusing [44]. In terms of preparation, because of its good gradient refractive index interval (1–1.4) and rotational symmetry, it can be designed easily by effective media theory using metamaterials [20,44]. However, the Lissajous lens, as well as the inverse Luneburg lenses and inversed Lissajous lenses, have non-rotationally symmetric or non-spherically symmetric refractive index distributions, which are more challenging to realize, especially in the 3D case. These lenses may be fabricated by 3D

printing technology, and it was reported that 3D printing can implement some custom 3D lenses [45]. For future applications, these asymmetric lenses are expected to be used to study 3D super-resolution imaging. Note that we also found interesting effects of virtual images in the inverse Luneburg lens, which are expected to be used in the integrated optical path of telescopes. In theory, these asymmetrical but closed trajectories imply the integrability of the optical system, and if such rule is broken, it may be helpful to study the optical chaos and chaotic switch [46]. In addition, due to the similarity of wave equations, the proposed non-spherically symmetric imaging lenses can be extended to acoustic and elastic waves.

Author Contributions: Conceptualization, D.G. and W.X.; methodology, D.G., W.X. and Y.G.; software, D.G. and W.X.; formal analysis, W.X., D.G., Y.G. and H.C.; investigation, D.G.; resources, D.G.; writing—original draft preparation, D.G.; writing—review and editing, W.X. and H.C.; supervision, H.C.; project administration, H.C.; funding acquisition, H.C. All authors have read and agreed to the published version of the manuscript.

Funding: This project is supported by the National Key Research and Development Program of China (Grants No. 2020YFA0710100, No. 2023YFA1407100) and the National Natural Science Foundation of China (Grant No. 12361161667).

Institutional Review Board Statement: Not applicable.

Informed Consent Statement: Not applicable.

Data Availability Statement: Data underlying the results presented in this paper are not publicly available at this time but may be obtained from the authors upon reasonable request.

Conflicts of Interest: The authors declare no conflicts of interest.

Methods

Below, we show the code of the ray tracing based on Hamiltonian optics, where *a*, *b*, and *c* are the three parameters in the refractive index formula for a 3D Lissajous lens. The starting point of a ray is (x_0, y_0, z_0) and the initial wave vector of the ray is (kx_0, ky_0, kz_0). n is the set refractive index distribution. The ode45 function is used to solve the differential equations and the Plot3 function is used to plot the 3D ray trajectory.

```
function particle_trajectory()
    % Define constants
    a = 1;
    b = 2;
    c = 2;

    % Initial conditions
    x0 = 1;
    y0 = 1;
    z0 = 1;
    kx0 = −0.5;
    ky0 = 1;
    kz0 = 0;

    % Time span
    tspan = [0 100];

    % Initial state vector
    initial_conditions = [x0 y0 z0 kx0 ky0 kz0];

    % Solve the system of differential equations
    [t, sol] = ode45(@(t, vars) odefunc(t, vars, a, b, c), tspan, initial_conditions);
```

```
    % Extract solutions
    x = sol(:, 1);
    y = sol(:, 2);
    z = sol(:, 3);

    % Plot the trajectory
    plot3(x, y, z, 'r', 'LineWidth', 2);
    xlabel('x');
    ylabel('y');
    zlabel('z');
    grid on;
    axis equal;
    box on;
    title('Particle Trajectory');
end
function dvarsdt = odefunc(~, vars, a, b, c)
    % Unpack variables
    x = vars(1);
    y = vars(2);
    z = vars(3);
    kx = vars(4);
    ky = vars(5);
    kz = vars(6);

    % Refractive index
    n = sqrt(2 - (x/a)^2 - (y/b)^2 - (z/c)^2);

    % Magnitude of the wave vector
    k_mag = sqrt(kx^2 + ky^2 + kz^2);

    % Derivatives of the refractive index
    Dx = -x/(a^2 * n);
    Dy = -y/(b^2 * n);
    Dz = -z/(c^2 * n);

    % Define the differential equations
    dxdt = 1/n * kx/k_mag;
    dydt = 1/n * ky/k_mag;
    dzdt = 1/n * kz/k_mag;
    dkxdt = k_mag/n^2 * Dx;
    dkydt = k_mag/n^2 * Dy;
    dkzdt = k_mag/n^2 * Dz;

    % Return the derivatives
    dvarsdt = [dxdt; dydt; dzdt; dkxdt; dkydt; dkzdt];
end
```

References

1. Pendry, J.B.; David, S.; David, R.S. Controlling electromagnetic fields. *Science* **2006**, *312*, 1780–1782. [CrossRef] [PubMed]
2. Leonhardt, U. Optical conformal mapping. *Science* **2006**, *312*, 1777–1780. [CrossRef]
3. Chen, H.; Hou, B.; Chen, S.; Ao, X.; Wen, W.; Chan, C.T. Design and experimental realization of a broadband transformation media field rotator at microwave frequencies. *Phys. Rev. Lett.* **2009**, *102*, 183903. [CrossRef] [PubMed]
4. Chen, H.; Chan, C.T. Transformation media that rotate electromagnetic fields. *Appl. Phys. Lett.* **2007**, *90*, 241105. [CrossRef]
5. Zang, X.; Jiang, C. Two-dimensional elliptical electromagnetic superscatterer and superabsorber. *Opt. Express* **2010**, *18*, 6891–6899. [CrossRef] [PubMed]
6. Narimanov, E.E.; Kildishev, A.V. Optical black hole: Broadband omnidirectional light absorber. *Appl. Phys. Lett.* **2009**, *95*, 041106. [CrossRef]
7. Greenleaf, A.; Kurylev, Y.; Lassas, M.; Uhlmann, G. Electromagnetic Wormholes and Virtual Magnetic Monopoles from Metamaterials. *Phys. Rev. Lett.* **2007**, *99*, 183901. [CrossRef]

8. Kadic, M.; Dupont, G.; Enoch, S.; Guenneau, S. Invisible waveguides on metal plates for plasmonic analogs of electromagnetic wormholes. *Phys. Rev. A* **2014**, *90*, 043812. [CrossRef]
9. Sheng, C.; Bekenstein, R.; Liu, H.; Zhu, S.; Segev, M. Wavefront shaping through emulated curved space in waveguide settings. *Nat. Commun.* **2016**, *7*, 10747. [CrossRef]
10. Pendry, J.B. Negative refraction makes a perfect lens. *Phys. Rev. Lett.* **2000**, *85*, 3966. [CrossRef]
11. Leonhardt, U. Perfect imaging without negative refraction. *New J. Phys.* **2009**, *11*, 093040. [CrossRef]
12. Blaikie, R.J. Comment on Perfect imaging without negative refraction. *New J. Phys.* **2010**, *12*, 058001. [CrossRef]
13. Leonhardt, U. Reply to comment on 'Perfect imaging without negative refraction'. *New J. Phys.* **2010**, *12*, 058002. [CrossRef]
14. Kinsler, P.; Favaro, A. Comment on Reply to comment on "Perfect imaging without negative refraction". *New J. Phys.* **2011**, *13*, 028001. [CrossRef]
15. Leonhardt, U. Reply to Comment on Reply to Comment on Perfect Imaging without Negative Refraction. *arXiv* **2010**, arXiv:1010.4161.
16. Leonhardt, U.; Philbin, T.G. Perfect imaging with positive refraction in three dimensions. *Phys. Rev. A* **2010**, *81*, 011804. [CrossRef]
17. Badri, S.H.; Gilarlue, M.M.; Taghipour-Farshi, H. Rectangular Maxwells fisheye lens via transformation optics as a crossing medium for dissimilar waveguides. *JOSB* **2020**, *37*, 2437–2443. [CrossRef]
18. Mateo-Segura, C.; Dyke, A.; Dyke, H.; Haq, S.; Hao, Y. Flat Luneburg lens via transformation optics for directive antenna applications. *IEEE Trans. Antennas Propag.* **2014**, *62*, 1945–1953. [CrossRef]
19. Synge, J.L. The absolute optical instrument. *Trans. Am. Math. Soc.* **1938**, *44*, 32–46. [CrossRef]
20. Zhou, Y.; Hao, Z.; Zhao, P.; Chen, H. Solid Immersion Maxwell's Fish-Eye Lens Without Drain. *Phys. Rev. Appl.* **2022**, *17*, 034039. [CrossRef]
21. Li, D.; Zhu, S.; Zhang, M.; Nian, Y.; Zhao, M.; Chen, X.; Yi, J. Synthetic Beam Scanning and Super-Resolution Coincidence Imaging Based on Randomly Excited Antenna Array. *IEEE Trans. Geosci. Remote Seng.* **2023**, *61*, 2002414. [CrossRef]
22. Lin, M.; Ratni, B.; Qi, P.; Yi, J.; André, L.; Shah, N.B. Flexible Generation and Manipulation of Microwave Bottle Beam Using a Reconfigurable Metamirror. *Adv. Photo. Res.* **2023**, *4*, 2300156. [CrossRef]
23. Miñano, J.C. Perfect imaging in a homogeneous three-dimensional region. *Opt. Express* **2006**, *14*, 9627–9635. [CrossRef]
24. Chen, H. Imaging along conformal curves. *Phys. Rev. A* **2018**, *98*, 043843. [CrossRef]
25. Chen, J.; Su, G.; Xu, S.; Chen, M.; Liu, Y.; Fang, D.; Zhou, J. Ultrabroadband and Multifunctional Achromatic Mikaelian Lens on an Elastic Plate. *Phys. Rev. Appl.* **2022**, *18*, 064047. [CrossRef]
26. Chen, H.; Xiao, W. The Morse lens. *Chin. Opt. Lett.* **2020**, *18*, 062403. [CrossRef]
27. Tyc, T.; Danner, A. Frequency spectra of absolute optical instruments. *New J. Phys.* **2012**, *14*, 085023. [CrossRef]
28. Tyc, T. Spectra of absolute instruments from the WKB approximation. *New J. Phys.* **2013**, *15*, 065005. [CrossRef]
29. Tyc, T.; Danner, A. Absolute optical instruments, classical superintegrability, and separability of the Hamilton-Jacobi equation. *Phys. Rev. A* **2017**, *96*, 053838. [CrossRef]
30. Tyc, T.; Herzánová, L.; Šarbort, M.; Bering, K. Absolute instruments and perfect imaging in geometrical optics. *New J. Phys.* **2011**, *13*, 115004. [CrossRef]
31. Fonseca, N.J.G.; Liao, Q.; Quevedo-Teruel, O. Equivalent planar lens ray-tracing model to design modulated geodesic lenses using non-Euclidean transformation optics. *IEEE Trans. Antennas Prag.* **2020**, *68*, 3410–3422. [CrossRef]
32. Chen, Q.; Horsley, S.A.R.; Fonseca, N.J.G.; Tyc, T.; Quevedo-Teruel, O. Double-layer geodesic and gradient-index lenses. *Nat. Commun.* **2022**, *13*, 2354. [CrossRef]
33. Šarbort, M.; Tyc, T. Spherical media and geodesic lenses in geometrical optics. *J. Opt.* **2012**, *14*, 075705. [CrossRef]
34. Tyc, T.; Dao, H.L.; Danner, A.J. Absolute optical instruments without spherical symmetry. *Phys. Rev. A* **2015**, *92*, 053827. [CrossRef]
35. Blair, D.E. *Inversion Theory and Conformal Mapping*; American Mathematical Society: Ann Arbor, MI, USA, 2000.
36. Junqueira, M.A.; Gabrielli, L.H.; Beltrán-Mejía, F.; Spadoti, D.H. Three-dimensional quasi-conformal transformation optics through numerical optimization. *Opt. Express* **2016**, *24*, 16465. [CrossRef] [PubMed]
37. Silva, D.G.; Teixeira, P.A.; Gabrielli, L.H.; Beltrán-Mejía, F.; Spadoti, D.H. Full three-dimensional isotropic carpet cloak designed by quasi-conformal transformation optics. *Opt. Express* **2017**, *25*, 23517–23522. [CrossRef]
38. Leonhardt, U.; Philbin, T. *Geometry and Light: The Science of Invisibility*; Courier Corporation: North Chelmsford, MA, USA, 2010.
39. Kravtsov, A.Y.; Orlov, Y.I. *Geometrical Optics of Inhomogeneous Media*; Springer: Berlin/Heidelberg, Germany; Moscow, Russia, 1990.
40. Schurig, D.; Pendry, J.B. Smith D R. Calculation of material properties and ray tracing in transformation media. *Opt. Express* **2006**, *14*, 9794–9804. [CrossRef]
41. Peng, H.; Han, H.; He, P.; Xia, K.; Zhang, J.; Li, X.C.; Bao, Q.L.; Chen, Y.; Chen, H. The Luneburg–Lissajous lens. *EPL* **2020**, *129*, 64001. [CrossRef]
42. Foster, R.; Nagarkoti, D.; Gao, J.; Benjamin, V.; Felix, N.; Spooner, C.; Haq, S.; Yang, H. Beam-steering performance of flat Luneburg lens at 60 GHz for future wireless communications. *Int. J. Antennas Propag.* **2017**, *2017*, 7932434. [CrossRef]
43. Xue, L.; Fusco, V.F. 24 GHz automotive radar planar Luneburg lens. *IET Microw. Antennas Propag.* **2007**, *1*, 624–628. [CrossRef]
44. Zhao, Y.Y.; Zhang, Y.L.; Zheng, M.L.; Dong, X.Z.; Duan, X.M.; Zhao, Z.S. Three-dimensional Luneburg lens at optical frequencies. *Laser Photon. Rev.* **2016**, *10*, 665–672. [CrossRef]

45. Rebecca, D.S.; Timothy, D.Y.; Koroush, S.; Du, T.N.; Nikola, A.D.; Jason, M.O.; Michael, A.J.; Oscar, D.H.; Frederick, J.R.; Lana, L.W. 3D printed gradient index glass optics. *Sci. Adv.* **2020**, *6*, 47.
46. Xu, C.; Dana, I.; Wang, L.G.; Sebbah, P. Light chaotic dynamics in the transformation from curved to flat surfaces. *Proc. Natl. Acad. Sci. USA* **2022**, *119*, e2112052119. [CrossRef] [PubMed]

Disclaimer/Publisher's Note: The statements, opinions and data contained in all publications are solely those of the individual author(s) and contributor(s) and not of MDPI and/or the editor(s). MDPI and/or the editor(s) disclaim responsibility for any injury to people or property resulting from any ideas, methods, instructions or products referred to in the content.